

An in vitro spinal cord injury model to screen neuroregenerative materials

Item Type	Article
Authors	Weightman, Alan P.;Pickard, Mark R.;Yang, Ying;Chari, Divya M.
Citation	Weightman, A. P., Pickard, M. R., Yang, Y., & Chari, D. M. (2014). An in vitro spinal cord injury model to screen neuroregenerative materials. <i>Biomaterials</i> , 35(12), 3756-3765. DOI: 10.1016/j.biomaterials.2014.01.022
DOI	10.1016/j.biomaterials.2014.01.022
Publisher	Elsevier
Journal	Biomaterials
Download date	2026-05-21 17:39:01
Link to Item	http://hdl.handle.net/10034/604949

1 A 'spinal cord injury in a dish' model to screen
2
3
4
5 neuroregenerative materials
6
7
8

9
10 *Alan P. Weightman*^{†‡}, *Mark R. Pickard*[†], *Ying Yang*[‡], and *Divya M. Chari*^{†*}
11

12
13 †Cellular and Neural Engineering Group, Institute for Science and Technology in Medicine,
14 Huxley Building, Keele University, Keele, Staffordshire, ST5 5BG, UK
15

16
17
18 ‡ Guy Hilton Research Centre, Institute for Science and Technology in Medicine,
19 Thornburrow Drive, Keele University, Staffordshire, ST4 7QB, UK
20
21

22
23
24
25 *To whom correspondence should be addressed. Phone: +44 1782 733314. Fax: +44 1782
26 733516. E-mail: d.chari@keele.ac.uk.
27
28
29
30
31
32
33
34
35
36
37
38
39
40
41
42
43
44
45
46
47
48
49
50
51
52
53
54
55
56
57
58
59
60
61
62
63
64
65

Abstract

1
2
3 Implantable ‘structural bridges’ based on nanofabricated polymer scaffolds have great
4
5
6 promise to aid spinal cord regeneration. Their development (optimal formulations, surface
7
8
9 functionalizations, biocompatibility, topographical influences and degradation profiles) is
10
11 heavily reliant on live animal injury models. These have several disadvantages including
12
13
14 invasive surgical procedures, ethical issues, high animal usage, technical complexity and
15
16
17 expense. *In vitro* 3-D organotypic slice arrays could offer a novel solution to overcome these
18
19
20 challenges, but their utility for nanomaterials testing is undetermined. We have developed an
21
22
23 *in vitro* model of spinal cord injury that replicates stereotypical cellular responses to
24
25
26 neurological injury *in vivo*, viz. reactive gliosis, microglial infiltration and limited nerve fibre
27
28
29 outgrowth. We describe a facile method to safely incorporate aligned, poly-lactic acid
30
31
32 nanofiber meshes (\pm poly-lysine + laminin coating) within injury sites using a lightweight
33
34
35 construct. Patterns of nanotopography induced outgrowth/alignment of astrocytes and
36
37
38 neurons in the ‘dish model’ were strikingly similar to that induced by comparable materials in
39
40
41 related studies *in vivo*. This highlights the value of our model in providing biologically-
42
43
44 relevant readouts of the regeneration-promoting capacity of synthetic bridges within the
45
46
47 complex environment of spinal cord lesions. Our approach can serve as a prototype to
48
49
50 develop versatile bio-screening systems to identify materials/combinatorial strategies for
51
52
53 regenerative medicine, whilst reducing live animal experimentation.

54
55
56
57
58
59
60
61
62
63
64
65
Keywords: organotypic slice culture, spinal cord injury, *in vitro* model, electrospinning,
aligned nanofiber, 3 R’s.

1. Introduction

1
2 The implantation of nanofiber scaffolds to serve as synthetic ‘*structural bridges*’ is an
3
4 approach with high regenerative potential following injury in a range of tissue systems,
5
6 notably spinal cord injury (SCI) [1]. The latter is a destructive, multifaceted condition, with a
7
8 poor clinical prognosis for functional recovery [2,3]. Strategically, such scaffolds can aid
9
10 regeneration by providing aligned topographies, gradients of chemical guidance cues and
11
12 transplant cell populations to replace lost/damaged cells [4–6]. Evaluation and optimization
13
14 of synthetic bridges is currently the subject of intensive research globally, with the
15
16 developmental testing of novel scaffolds and constructs being heavily reliant on live animal
17
18 injury models [7].
19
20
21
22
23

24 There are several ethical and practical drawbacks relating to animal experimentation in this
25
26 context. The production of injury models can be a highly invasive and time consuming
27
28 process, usually requiring high technical expertise. Depending on the model, the procedures
29
30 can result in serious adverse effects such as infections, paralysis or other movement
31
32 disorders, bladder dysfunction and so on [7]. Even in the hands of a skilled operator, surgical
33
34 procedures can inherently generate significant inter-animal variability, requiring large animal
35
36 group sizes for statistical validity [7]. Following lesion (injury) induction, introduction of
37
38 synthetic scaffolds into injury areas usually requires re-anesthetization, with the second
39
40 procedure involving similar risks to injury induction. *In vivo* models necessitate the use of
41
42 analgesia and rigorous post-operative monitoring of animals, which must be housed
43
44 individually [8]. The requirements for specialist staff and infrastructure in particular, place
45
46 major financial constraints on such work [9,10].
47
48
49
50
51
52

53 Considerations of this nature have prompted the current global drive for the Reduction,
54
55 Replacement and Refinement of animal experimentation (the 3R’s principles) [11]. In
56
57 particular, there is a major current need to develop facile, high throughput *in vitro* models
58
59
60
61
62
63
64
65

1 that: (i) mimic pathological features of injury sites *in vivo* (and therefore have biological
2 validity); (ii) are compatible with introduction of nano-engineered constructs for the robust
3 and reproducible testing of the latter; and (iii) induce comparable cellular responses to the
4 introduced materials as those in live animal injury models [12].
5
6
7

8
9 Models possessing such features can be predicted to reduce animal usage and suffering, as
10 well as costs and technical difficulty, thereby facilitating the screening of pro-regenerative
11 materials for nanomedicine. Despite the need for such biologically relevant testing systems,
12 ‘*reductionist models*’ described to-date typically lack the ability to mimic multifaceted
13 components of SCI pathology and the complexities of cytoarchitecture *in vivo*. The central
14 nervous system (CNS; i.e. the brain and spinal cord) is a particularly challenging tissue
15 system in this regard, due to the complex cellular dynamics and intricate (cardinal)
16 pathophysiological events displayed after neurological injury [13]. For example, following
17 SCI *in vivo*: astrocytes upregulate expression of the astrocyte-specific marker glial fibrillary
18 acidic protein (GFAP), within and adjacent to lesions, to form a scar that constitutes a critical
19 barrier to axonal regeneration [14]; microglia (the immune-competent cells of the CNS)
20 infiltrate into lesion sites and are responsible for the breakdown and phagocytosis of cellular
21 debris and toxic substances following injury [15,16]; and limited, spontaneous sprouting of
22 nerve fibers occurs from lesion margins, with the extent of regeneration declining with age
23 [17].
24
25
26
27
28
29
30
31
32
33
34
35
36
37
38
39
40
41
42
43
44

45 In this context, 3-D, multicellular organotypic slice cultures (slices of immature tissue that
46 develop comparably to the donor organ in an *ex vivo* environment) could offer a unique
47 solution to the above challenges. For example, such tissue arrays are increasingly being used
48 for long term, high throughput assays in experimental neurology [18]. They provide a
49 versatile bridge between isolated cell culture and *in vivo* experiments wherein the
50 cytoarchitecture and structural relationships of cells are maintained, allowing for parameters
51
52
53
54
55
56
57
58
59
60
61
62
63
64
65

1 of neural regeneration, e.g. neuronal survival [19], nerve fiber regeneration [20,21] and
2 collateral axon sprouting to be evaluated [22]. These models offer several advantages
3 including the ease of manipulation/observation of *in vitro* preparations [18]; several ages,
4 neuroanatomical areas and species, including human foetuses [23] and transgenic models
5 [24,25] can be used as tissue donor sources, offering high flexibility to study neural
6 pathologies and disease mechanisms. Slice cultures are amenable to electrophysiological
7 techniques [26], molecular biology methods [27], time lapse video microscopy [28] and
8 dynamic confocal imaging [10,29,30], which has greatly expanded the translational utility of
9 this approach. Clearly therefore, such models have wide applicability to a range of tissues and
10 pathologies. Despite their critical advantages, to the best of our knowledge, such models have
11 never been utilized to examine the interactions of nano-materials with cells in an injury-
12 simulated environment.

13
14 To address this issue, we have established a prototype slice model *in vitro*, which combines
15 for the first time, a tissue injury paradigm with delivery of pro-regenerative scaffolds. To
16 achieve this, we first describe a reproducible method to induce a focal injury in spinal cord
17 slices; the basic pathological features of these injuries *in vitro* have been evaluated to
18 establish their overall relevance to *in vivo* pathology. We then present a novel methodology
19 to incorporate aligned nanofiber scaffolds across injury foci to evaluate the topographical
20 influence on neural cell responses within injury sites.

21 22 **2. Materials and Methods**

23
24
25 **2.1. Materials.** Tissue culture plastics, culture media and supplements were from Sigma-
26 Aldrich (Poole, UK) and Fisher Scientific (Loughborough, UK). Omnipore membranes
27 (JHWP04700) and Millicell culture inserts were from Millipore (Watford, UK). The
28 live/dead cell viability kit was from Invitrogen (Paisley, UK) and Vectashield mounting
29
30
31
32
33
34
35
36
37
38
39
40
41
42
43
44
45
46
47
48
49
50
51
52
53
54
55
56
57
58
59
60
61
62
63
64
65

1 medium with DAPI (4', 6-diamidino-2-phenylindole) from Vector Laboratories
2 (Peterborough, UK). Primary antibodies were: rabbit and mouse anti-neuronal class III β -
3 tubulin (clone TUJ-1, Covance, Princeton, NJ), rabbit anti-GFAP (DakoCytomation, Ely,
4 UK), biotin-conjugated anti-lectin (from *Lycopersicon esculentum*, tomato; Sigma-Aldrich,
5 UK). Cy3- and FITC-conjugated AffiniPure secondary antibodies were from Jackson
6
7
8
9
10
11
12
13
14
15
16
17
18
19
20
21
22
23
24
25
26
27
28
29
30
31
32
33
34
35
36
37
38
39
40
41
42
43
44
45
46
47
48
49
50
51
52
53
54
55
56
57
58
59
60
61
62
63
64
65

ImmunoResearch Laboratories Inc. (West Grove, PA, USA); FITC-conjugated anti-biotin secondary antibody was from Sigma-Aldrich (UK). Poly-L,D-lactic acid (PLA; 96% L: 4% D) was from Purac biochem BV (Gorinchem, Netherlands) and chloroform, dimethylformamide and rhodamine B from Sigma-Aldrich (UK). Collagen type I solution was from BD Biosciences (UK).

2.2. Production of Organotypic Spinal Cord Slice Cultures. The care and use of animals was in accordance with the Animals (Scientific Procedures) Act of 1986 (United Kingdom) with local ethics committee approval. Spinal cords derived from mouse pups aged 0 - 6 postnatal days (P0 - P6) were rapidly removed after decapitation and transferred into ice-cold slicing medium (EBSS buffered with 25mM HEPES) [31–33]. Longitudinal slices (350 μ m) were prepared using a McIlwain tissue chopper. Two/three slices were transferred to Omnipore membrane ‘confetti,’ resting on the Millicell culture insert membrane. Slices were cultured at the air-medium interface with culture medium (50% MEM, 25% heat-inactivated horse serum, 25% EBSS supplemented with 36 mM D-glucose, 100 U/mL penicillin, 100 μ g/mL streptomycin and 250 ng/mL amphotericin B) for up to 16 days *in vitro* (DIV; Figure 1A1 and A2). Cultures were incubated in humidified 95% O₂/5% CO₂ at 37°C with 80% medium changes every two days. In all cases the number of experiments, *n*, refers to slices obtained across different animals and litters.

1
2
3
4
5
6
7
8
9
10
11
12
13
14
15
16
17
18
19
20
21
22
23
24
25
26
27
28
29
30
31
32
33
34
35
36
37
38
39
40
41
42
43
44
45
46
47
48
49
50
51
52
53
54
55
56
57
58
59
60
61
62
63
64
65

2.3. Immunocytochemistry. Slices were washed in phosphate buffered saline (PBS) before and after fixation with 4% paraformaldehyde [PFA; 20 min; room temperature (RT)]. Samples were incubated in blocking solution consisting of 5% normal donkey serum (10% for lectin antibodies) in PBS, with 0.3% Triton X-100 for TUJ-1 and GFAP staining (30 min; RT). Incubations with primary antibodies in blocking solution followed (lectin 1:200, GFAP 1:500; TUJ-1 1:1000; 24 hours at RT or 4°C). Following PBS washes samples were incubated with appropriate Cy3- and/or- FITC-conjugated secondary antibodies (4 h at RT or 4°C). Slices were subsequently washed with PBS and mounted with Vectashield mounting medium containing DAPI.

2.4. Fluorescence Imaging and Statistical Analysis. Slices were visualized on an Axio Scope A1 fluorescence microscope (Carl Zeiss MicroImaging GmbH; Germany) fitted with an Axio Cam ICc1 digital camera and AxioVision software. Where applicable, fluorescence images of immunostained slices were merged using Photoshop CS5.1 (version 12.1). GraphPad Prism v5.0 software was used for all statistical analyses performed. All values quoted are expressed as the mean \pm standard error of the mean (SEM), unless otherwise stated. Data were analyzed by a one-way analysis of variance, using Bonferroni's multiple comparison test for post-hoc analysis; a Bartlett's test was performed to examine homogeneity of variance and, where necessary, data were transformed (square root or log) prior to analysis.

2.5. Assessment of Organotypic Spinal Cord Slice Viability after *In Vitro* Culture. For live/dead assays, intact slices (P0 - P5; n = 3) cultured for 6 – 16 DIV were washed three times with PBS. Slices were incubated with calcein (1 μ L/mL) to label live cells and ethidium bromide (3 μ L/mL) to label dead cells, for 15 minutes at 37°C. Following PBS

1 washes, slices were mounted with Vectashield mounting medium containing DAPI.
2
3 Fluorescence micrographs of staining were captured with consistent exposure settings. The
4
5 corrected integrated density (Supporting Information S1) was quantified using ImageJ
6
7 software (version 1.45s; NIH) and the values for the live-stained micrograph expressed as a
8
9 percentage of the sum total from both [30].
10

11
12
13 **2.6. Lesioning Organotypic Spinal Cord Slice Cultures.** To develop a reproducible focal
14
15 lesioning method, a slice lesioning tool was developed in-house using a pre-assembled,
16
17 double-bladed scalpel (Figure 1B). This was the product of several prototypes optimized to
18
19 rapidly produce regular, evenly spaced lesion margins, whilst preventing drying of slices. The
20
21 tool was aseptically assembled prior to lesioning by taping together two surgical blades (size
22
23 15) secured into an empty scalpel holder (Figure 1B). To assess the reproducibility of
24
25 lesioning tool construction, the diameter of lesions induced in slices was investigated across
26
27 five litters (3 - 14 slices per litter; each litter representing independent assembly of the tool).
28
29 Fluorescence micrographs of DAPI-stained slices were used to calculate the mean distance
30
31 between lesion margins from each culture.
32
33
34
35
36
37

38
39 The lesioning procedure was implemented inside a laminar flow hood using a dissection
40
41 microscope at x12.5 magnification. To improve lesioning reproducibility, the shape of the
42
43 confetti supporting slices (see Figure 1A3 and section 2.2) was re-designed to facilitate the
44
45 use of forceps to grip both the culture insert wall and confetti together, thus stabilizing the
46
47 slice. The lesioning tool was drawn through the slice and small lateral movements used to
48
49 ensure the complete severing of nerve fiber tracts. The slice debris between the two lesion
50
51 margins was subsequently removed using an aspirator, fitted with a 200 μ l pipette tip.
52
53
54
55
56 Cultures were lesioned at 1 - 8 DIV and were fixed within 7 days of lesioning. Slices
57
58 generated in spinal cords derived from both 'younger' (P0 mice: lesioned after 1 DIV; fixed 7
59
60
61
62
63
64
65

1 days later) and ‘older’ (P5 mice: lesioned after 8 DIV; fixed 7 days later) slices with different
2 extents of intrinsic nerve fiber outgrowth were used for characterizing the interaction of
3
4 nanofibers with neuronal cells.
5
6
7
8

9 **2.7. Quantification of Astrogliosis at Lesion Margins** (Supporting Information S2). P0 - P2

10 slice cultures lesioned after 1 DIV, were fixed at 6 days post-lesioning and stained for GFAP.

11 Slices were imaged with consistent exposure settings and converted to grayscale. Optical

12 density (OD) profiles from the lesion margins were generated using ImageJ software and

13 averaged to form a single profile for each slice. Baseline intensity values were obtained at *ca*

14 1mm from the lesion site, where astrocytes displayed un-reactive morphologies and lower

15 GFAP expression levels. A single, corrected OD profile from the lesion margins of each slice

16 (n = 6) was produced by subtracting the baseline intensity from each value in the averaged

17 trace and averaged with traces from five other slices. The differences in average OD in the

18 zones 0 - 100 μm , 100 - 200 μm and > 200 μm from the lesion boundary were subsequently

19 compared.
20
21
22
23
24
25
26
27
28
29
30
31
32
33
34
35
36
37
38

39 **2.8. Quantification of Microglial Infiltration into Lesion Sites.** Spinal cords were extracted

40 from P0 - P2 mice, lesioned after 2 DIV and fixed 0, 5 and 10 days post-lesioning. The

41 numbers of lectin-positive (lectin⁺) microglia were counted within the lesion site of each

42 slice, using a standard size grid overlaid onto each image. The total number of microglia per

43 unit area per slice was averaged at each time point (n = 3).
44
45
46
47
48
49
50
51
52

53 **2.9. Fabrication and Characterization of Electrospun Nanofibers.** A 2% (w/v) PLA

54 solution was prepared by dissolving the polymer in chloroform prior to the addition of

55 dimethylformamide (7:3 solvent volume ratio). The addition of rhodamine B into the solution
56
57
58
59
60
61
62
63
64
65

1 (0.1 mg/mL) produced fluorescent nanofibers. A parallel electrode collector (Figure 1C1)
2 was used to obtain nanofibers in a highly aligned conformation over a 10 minute unit
3 operation. Electrospinning parameters were kept constant for all experiments. A
4 'densification' tool (Figure 1C2) was used as an intermediate processing step, to compact the
5 nanofibers from the nanofiber deposition area of the collector (84 cm²) to that of the tool (13
6 cm²), whilst maintaining the aligned nanofiber conformation. Nanofibers were then mounted
7 onto acetate frames from the densification tool (Figure 1C3) and affixed using a spray
8 adhesive, to be handleable and to maintain their aligned conformation for use in experiments.
9 Nanofibers were desiccated overnight and sterilized in a UV chamber before use in all
10 experiments.
11
12
13
14
15
16
17
18
19
20
21
22
23

24 The diameter and line density (number of aligned nanofibers along a distance perpendicular
25 to the axis of nanofiber orientation) of both fluorescent and non-fluorescent nanofibers used
26 were determined from micrographs taken with a field emission scanning electron microscope
27 (Supporting Information S3).
28
29
30
31
32
33
34
35

36 **2.10. Nanofiber Surface Treatment with Poly-D-Lysine and Laminin.** Multiple sterile,
37 portable nanofiber frames were rapidly incubated with poly-D-lysine and laminin solutions
38 (herein termed PDL and LAM, respectively) on a chamber developed in-house (Figure 1C4).
39 Coating solutions were applied sequentially (20 µg/mL PDL: 12 hours; 10 µg/mL LAM: 5
40 hours) then washed with PBS and kept moist for placement over slice lesions. Fourier
41 transform infrared spectroscopic analysis confirmed the presence of protein on the surface of
42 treated nanofibers, verifying surface treatment procedures (Supporting Information S4).
43
44
45
46
47
48
49
50
51
52
53
54
55

56 **2.11. Incorporation of Nanofibers over Lesioned Slices.** The technical challenge of
57 incorporating delicate, aligned nanofibers over lesioned slices (Figure 1C5) was overcome by
58
59
60
61
62
63
64
65

1 gently positioning nanofiber-bearing frames parallel to the slice longitudinal axis using
2 forceps. A 3 mg/mL neutralized collagen solution was applied around the acetate frame, to
3 ensure stability for subsequent staining procedures.
4
5
6
7
8

9 **2.12. Axonal Outgrowth and Alignment across Lesions (\pm Nanofibers).** Spinal cords
10 derived from both ‘younger’ (P0 mice: lesion at 1 DIV) and ‘older’ (P5 mice: lesion at 8
11 DIV) models were used to evaluate intrinsic nerve fiber outgrowth. Nerve fiber outgrowth
12 density was quantified in TUJ-1 stained slices from both models \pm nanofibers (Supporting
13 Information S5). Fluorescence micrographs were obtained and OD profiles generated from
14 regular intervals along the length of the lesion site using ImageJ software for peak analysis
15 (Supporting Information S5). The average total number of peaks per mm^2 was then calculated
16 for each slice ($n \geq 3$).
17
18
19
20
21
22
23
24
25
26
27

28 To assess the alignment of TUJ-1⁺ nerve fibers with coated and uncoated nanofibers, the
29 percentage of aligned TUJ-1⁺ nerve fibers was scored ($n \geq 3$ per group) by two independent
30 assessors blind to the treatment groups: five data bins, each with a range of 20%, were used
31 to classify any potential alignment observed.
32
33
34
35
36
37
38
39
40

41 **3. Results**

42 **3.1. Slice Preparation and Lesion Induction**

43 The viability of intact slices quantified using fluorescence microscopy (Supporting
44 Information S1) was found to be approximately $96\% \pm 2\%$, with a representative slice shown
45 in Figure 2A. Dead cells generated by the slicing procedure were typically found at the slice
46 edges [34].
47
48
49
50
51
52
53
54
55
56
57
58
59
60
61
62
63
64
65

1
2
3
4
5
6
7
8
9
10
11
12
13
14
15
16
17
18
19
20
21
22
23
24
25
26
27
28
29
30
31
32
33
34
35
36
37
38
39
40
41
42
43
44
45
46
47
48
49
50
51
52
53
54
55
56
57
58
59
60
61
62
63
64
65

Following the optimization of the lesioning procedure, a complete transecting lesion could be induced in slices with a double-bladed scalpel, ensuring the severing of nerve fibers across the lesion. In contrast, the use of single-blade cutting instruments, e.g. conventional scalpels, to produce the same injury requires two sequential transecting motions, which increases the procedural difficulty/duration and lesion size variability, whilst restricting the minimum possible lesion size to approximately 750 μm (data not shown). The tissue between the cut edges could be efficiently removed to reveal distinct lesion margins and to enable the visualization of regenerative events across lesion sites (Figure 2B). Measurements of induced lesions revealed a mean distance of 439 μm between lesion margins, which was highly reproducible ($\pm 4 \mu\text{m}$; coefficient of variation = 2 %) across five separate cultures, each representing separate occasions of tool assembly (Figure 2C). Increasing the inter-blade distance concomitantly increased the lesion area, thereby increasing the versatility of the injury model in terms of severity and to accommodate a range of potential scaffold sizes. Live/dead staining of lesioned slices 7 days post-injury (Figure 2D) demonstrated that the procedures did not significantly impact overall slice viability for further experimentation, as evidenced by a central band of live cells with few dead cells interspersed around the area of injury.

3.2. Characterization of Slice Lesion Pathology

Following the development of the lesioning procedure, a series of neuropathological assessments were performed to evaluate whether the following key pathological events known to occur *in vivo* were mimicked within slice lesions.

(i) *Increased astrocyte reactivity in lesion margins*: Clear and even GFAP staining was observed throughout slices; notably, GFAP⁺ cells at lesion margins were intensively reactive

1 and hypertrophic (Figure 3A) - hallmark features of the glial scar *in vivo* [35]. Quantification
2 of relative GFAP expression at slice lesion margins versus normal areas in the body of the
3 slice (Supporting Information S2), using mean fluorescence intensity profiles (Figure 3B; n =
4 6) revealed a significant intensity increase in the first 100 μm adjacent to lesion margins
5 (Figure 3C). Comparatively, in regions more distant to the lesion site, GFAP⁺ astrocytes with
6 normal, polygonal morphologies and lower fluorescence intensities were found.
7
8
9

10
11
12
13
14
15
16
17 *(ii) Microglial activation and infiltration into lesion sites:* Lectin positive (lectin⁺)
18 microglia were identified in immunostained slices and displayed activated morphologies
19 within the lesion site (Figure 3A). In contrast, resting microglia located in the main body of
20 slices exhibited numerous ramified processes. Counts of the numbers of lectin⁺ microglia
21 within the lesion sites of slices (n = 3 per time point) revealed a significant increase in the
22 number of microglia at 5 days post-lesioning (Figure 3D), with a decrease in number after 10
23 days.
24
25
26
27
28
29
30
31
32

33
34
35
36 *(iii) Age/time-dependent spectrum of intrinsic nerve fiber outgrowth from lesion margins:*
37 After seven days of culture, nerve fiber outgrowth in young slices was extensive and
38 randomly orientated (Figure 3E). By contrast the outgrowth in older slices was relatively
39 limited, but also with random orientations (Figure 3F).
40
41
42
43
44
45
46
47
48

49 **3.3. Incorporation of Nanofiber Scaffolds over Lesions and Topographical Influences** 50 **on Cells**

51 The introduction of rhodamine B into the PLA solution to fabricate fluorescent nanofibers
52 had no statistically significant (two-tailed Student's t-test) effect on either diameter (566 ± 20
53 nm *versus* 534 ± 5 nm for non-fluorescent nanofibers) or line density (534 ± 5 fibers / mm
54
55
56
57
58
59
60
61
62
63
64
65

1
2
3
4
5
6
7
8
9
10
11
12
13
14
15
16
17
18
19
20
21
22
23
24
25
26
27
28
29
30
31
32
33
34
35
36
37
38
39
40
41
42
43
44
45
46
47
48
49
50
51
52
53
54
55
56
57
58
59
60
61
62
63
64
65

versus 566 ± 20 fibers / mm for non-fluorescent nanofibers) of nanofibers produced (Supporting Information S3), highlighting reproducibility in nanofiber production/processing for all experiments.

Nanofibers were mounted onto acetate frames (Figure 4A), with both the fluorescence and alignment (Figure 4B) retained post-culture with lesioned slices (Figure 4C). The overall viability after incorporation of uncoated nanofiber scaffolds over lesioned slices (Figure 4D) remained high, with comparatively few dead cells present around the lesion site and within the body of the slice. Some evidence of cellular attachment to nanofibers across the lesion was also demonstrated (Figure 4D; white arrow heads), indicating nanofiber-slice contact over the culture period.

Evaluation of the topographical influence of the nanofabricated scaffolds on cells in lesion sites (using uncoated versus PDL-LAM coated fibers; $n \geq 3$ slices in each treatment group) showed that gliotic scar formation occurred similar to control slices (without nanofibers), with an intense region of GFAP expression at the first 100 μm of lesion margins. Following incorporation of uncoated nanofibers, no evidence of astrocyte attachment/alignment was observed (Figure 4E). In striking contrast, PDL-LAM coating of nanofibers induced extensive alignment of astrocytes, notably extending long thin processes (c.a. 100 - 200 μm) across the lesion site (Figure 4F). Extensive attachment of microglia to both uncoated (Figure 4G) and coated nanofibers was observed over lesion sites. Notably, elongated microglia were visible over the entire area of the slice in contact with nanofibers.

Quantification of the outgrowth (Supporting Information S5) and alignment of nerve fibers in both models of intrinsic regeneration showed that no significant nerve fiber attachment and outgrowth occurred (Figure 5A) following incorporation of uncoated nanofibers. In striking contrast, coated nanofibers enhanced nerve fiber outgrowth (Figure 5B), as confirmed by the mean nerve fiber outgrowth density (Figure 5C). Semi- quantitative assessment of the

1 alignment of nerve fibers on coated/uncoated nanofibers (Figure 5D) showed extensive
2 alignment in both lesion models on coated nanofibers: topographical effects appeared more
3 pronounced in the lesion model generated from P0 mice compared to that generated from P5
4 mice, where a greater incidence of interaction between nerve fibers and materials were
5 observed. Additionally, a sub-population of aligned cells displayed the morphological
6 phenotypes of spinal cord interneurons (Figure 5E). Occasionally, evidence of nerve fiber
7 extension coincident with elongated astrocytes was observed (Figure 5F), suggesting that a
8 component of nerve fiber elongation may occur secondary to topographical cues from aligned
9 astrocytes.
10
11
12
13
14
15
16
17
18
19
20
21
22
23

24 **4. Discussion**

25
26 *'Combinatorial'* neural tissue engineering strategies have been suggested to be essential to
27 promote various aspects of neural regeneration (such as nerve fiber regeneration, suppression
28 of scar formation and immune responses, promotion of blood vessel growth) within the
29 complex, multi-faceted pathology of SCI [36–40]. Such synergistic approaches have the
30 potential to regenerate the injured spinal cord with varying degrees of efficacy, but none have
31 been successfully translated into the clinic [41]. The full potential of combinatorial strategies
32 utilising aligned nanofibers with combinations of cells and biomolecules has yet to be
33 elucidated, due in part to a heavy reliance on *in vivo* SCI models, in the absence of high-
34 throughput, biologically-relevant *in vitro* screening models of SCI [5,42]. Two-dimensional
35 reductionist tools in current widespread use e.g. microfluidic devices, have provided useful
36 insights in tissue engineering, as these permit the study of fundamental, isolated aspects of
37 neuronal regeneration and response to materials/biomolecules post-injury [43,44]. However,
38 such *in vitro* models lack simulation of more complex multicellular pathology, within a
39
40
41
42
43
44
45
46
47
48
49
50
51
52
53
54
55
56
57
58
59
60
61
62
63
64
65

1 relevant extracellular injury environment, for detailed readouts of the biological response to
2 materials.
3

4 By contrast, we consider that the SCI model developed here can be exploited to address
5 this important technological gap. First, 5-7 spinal cord slices can be routinely obtained from a
6 single animal (depending on age), permitting the assessment of several conditions within the
7 same batch of slices, thereby reducing experimental variability and successfully addressing
8 the 3R's principles. Second, we demonstrate that three cardinal pathological features of SCI
9 *in vivo* can be mimicked in slice lesions, viz. post-traumatic astrogliosis, infiltration of lesions
10 by activated microglia (which is broadly comparable with their acute infiltration
11 characteristics *in vivo*) [33,48] and limited random outgrowth of nerve fibers from the lesion
12 margins of slices derived from older animals.
13
14
15
16
17
18
19
20
21
22
23
24

25
26 Third, the cellular responses observed in slice lesions following incorporation of PLA
27 scaffolds or laminin-coated scaffolds are comparable to published reports *in vivo*, using a
28 complete transecting injury model (a model used widely in experimental neurology to
29 evaluate regenerative strategies). PLA is approved for clinical use by the Food and Drug
30 Administration as it creates non-toxic waste products and has been widely used as a
31 scaffolding material in the tissue engineering research community. Uncoated PLA scaffolds
32 generally exhibit low levels of host neuronal regeneration and typically result in the
33 formation of a gliotic scar at the interface between host tissue and the implant [46–49]. By
34 contrast, the incorporation of laminin (or a suitable hydrogel e.g. fibrin [50]) into bridges
35 increases axon regeneration and disrupts gliotic scar formation *in vivo* [51–54]. PDL has
36 additional effects in promoting neuronal cell adhesion [55]. The decision to use both coatings
37 in this study was based on reports in the literature that suggest the attachment and extension
38 of neuronal processes is enhanced on PDL-LAM coated surfaces, compared to PDL alone
39 [56]. The extensive attachment of microglia to nanofibers bears resemblance to the activity of
40
41
42
43
44
45
46
47
48
49
50
51
52
53
54
55
56
57
58
59
60
61
62
63
64
65

1 microglia *in vivo* following transplantation of nanofiber scaffolds into SCI sites [57]. The
2 observation that cells in the 3-D slices can distinguish between different surface coatings
3 suggests that they are able to make sophisticated choices regarding material interactions,
4 within a complex environment *in vitro*. This highlights the high utility of our model in acting
5 as a reliable '*predictor*' of *in vivo* neural cell behaviours in response to various materials and
6 surface chemistries, and hence its value as a bio-screening method. Furthermore, this
7 suggests that the model can enable comparative investigations of various modifications to
8 enhance nerve fiber outgrowth and alignment, including: different polymer formulations and
9 other potentially efficacious substrates with an aligned topography; fiber densities and
10 diameters; scaffold functionalization with therapeutic biomolecules (promoting growth or
11 targeting major CNS inhibitors) and therapeutic stem/progenitor cell populations.
12

13
14 The combination of the portable and lightweight nanofiber meshes with supporting acetate
15 frames utilized in this study provide an innovative solution for determining the functional
16 utility of various nanofiber materials. The post-collection processing of aligned nanofibers to-
17 date has been heavily reliant on direct collection onto 2-D glass coverslips for mechanical
18 support, or alternatively, relatively thick, 3-D, more mechanically stable nanofiber meshes
19 have been utilized but have additional challenges regarding cellular infiltration throughout
20 the mesh thickness [1,58,59]. The supporting acetate frames: (i) provide mechanical stability
21 to the nanofibers; (ii) maintain nanofiber alignment throughout culture; (iii) obviate the
22 requirement for including a supporting substrate (e.g. a gel) to bridge the lesion gap, which
23 would add to the complexity of the construct and increase the difficulty of interpreting the
24 basic pro-regenerative readout of different nanofiber materials and surface treatments on
25 multiple neural populations across injury sites; and (iv) permit a choice of nanofiber density.
26 The density of nanofibers chosen in this study was fine tuned in order to: (i) provide
27 sufficient nanofiber surfaces for cells to interact with without obscuring the visualization of
28
29
30
31
32
33
34
35
36
37
38
39
40
41
42
43
44
45
46
47
48
49
50
51
52
53
54
55
56
57
58
59
60
61
62
63
64
65

1 cellular events in lesions and; (ii) reduce nanofiber clumping and hence retain the
2 topographical influence on neural cell populations. The development of a coating chamber
3 for these studies permits the efficient and sequential coating of multiple nanofiber frames in
4 suspension with different biomolecules.
5
6
7

8
9 In terms of the utility of the two models of different ages chosen for our study, the
10 extensive random nerve fiber outgrowth in younger slices is suited to the examination of
11 axonal outgrowth on bioengineered substrates with an aligned topography. By contrast, the
12 older slices that recapitulate cardinal neural features of traumatic injury in the adult CNS,
13 such as limited nerve fiber outgrowth, are suited to the examination of the regeneration-
14 enhancing properties of novel biomaterials. The spontaneous sprouting of nerve fibers
15 observed from the margins of lesioned spinal cord slices in this paradigm, which declines
16 with the age of donor tissue and is influenced by pre-lesioning culture time, has been reported
17 previously [31]. Further, functional assessments of regeneration i.e. electrophysiological
18 recordings may provide a more detailed readout of scaffold regeneration-enhancing
19 properties within this model [26]. Both models are suitable for studying the responses of the
20 non-neuronal, (supporting) glial cells in lesions. The nanofiber-induced morphological
21 reorganization of scar-forming astrocytes that normally form a critical barrier to nerve fiber
22 regeneration reveals a potential application of the injury model for screening efficacious
23 molecules and strategies that aim to disrupt the neuroglial scar, via the re-organization of
24 reactive astrocyte morphology. Further, the observed infiltration of microglial cells into
25 lesion sites indicates that acute inflammatory responses can be mimicked within the lesion
26 sites *in vitro*. Their activation in SCI can be a significant barrier to the development of
27 efficacious interventions as there is evidence implicating them as inhibitors of axonal
28 regeneration via expression of inhibitory guidance molecules such as Netrin-1 and repulsive
29 guidance molecules [60,61]. Microglial attachment to nanofibers provides an *in vitro* readout
30
31
32
33
34
35
36
37
38
39
40
41
42
43
44
45
46
47
48
49
50
51
52
53
54
55
56
57
58
59
60
61
62
63
64
65

1 for the optimization and testing of biocompatible materials and coatings that evoke minimal
2 inflammatory responses. It also demonstrates the potential for long-term studies, where
3 preliminary examination of the material degradation properties and breakdown mechanisms
4 may be assessed.
5
6
7
8

9 Whilst this study has utilized spinal cord as the test tissue, we consider that the high-
10 throughput model described here can serve as a prototype for the wider development of
11 highly versatile bio-screening systems for regenerative medicine/nanotechnology. We can
12 predict that these will allow for the identification of novel pro-regenerative materials for a
13 wide range of tissue applications, whilst significantly reducing reliance on live animal
14 experimentation, thereby accelerating the rate of discovery of nanotherapeutic agents for
15 tissue engineering (Figure 6).
16
17
18
19
20
21
22
23
24
25
26
27
28
29

30 **5. Conclusion**

31 We have developed a multicellular, *in vitro* model of spinal cord injury that mimics
32 multiple cardinal features of *in vivo* pathology. Functionalized nanofibers were able to induce
33 dramatic responses in multiple cell types in the injury sites; these are comparable to those
34 induced in live animal models. Our studies demonstrate the high potential of the model to
35 function as a prototype screening system for promising nanotherapeutic interventions, either
36 in isolation, or as part of a combinatorial treatment strategy. We can predict that the use of
37 higher-throughput *in vitro* models of SCI, such as the one we describe here, can aid in
38 overcoming a growing bottleneck in the therapeutic testing of promising new materials and
39 combinatorial therapies, whilst reducing the high current reliance on live animal testing.
40
41
42
43
44
45
46
47
48
49
50
51
52
53
54
55
56
57
58
59

60 **Acknowledgments**

61
62
63
64
65

1 This work is supported by the EPSRC Doctoral Training Centre in regenerative medicine
2 (EP/F500491/1). We would like to thank Dr. Ian Wimpenny for his help with electrospinning,
3
4 Dr. Paul Roach for conducting the FTIR analysis of nanofiber surface treatment and Jamie
5
6
7 Thurman-Newell for help designing the neuronal outgrowth density analysis.
8
9

10
11
12 The authors confirm that there are no known conflicts of interest associated with this
13
14 publication and there has been no significant financial support for this work that could have
15
16
17 influenced its outcome.
18
19
20
21
22
23
24
25
26
27
28
29
30
31
32
33
34
35
36
37
38
39
40
41
42
43
44
45
46
47
48
49
50
51
52
53
54
55
56
57
58
59
60
61
62
63
64
65

- 1 [1] Kubinová S, Syková E. Nanotechnologies in regenerative medicine. *Minim Invasive Ther Allied Technol* 2010;19:144–56.
- 2
- 3 [2] Hulsebosch CE. Recent advances in pathophysiology and treatment of spinal cord
4 injury. *Adv Physiol Ed* 2002;26:238–55.
- 5
- 6 [3] Silver J, Miller JH. Regeneration beyond the glial scar. *Nat Rev Neurosci* 2004;5:146–
7 56.
- 8
- 9 [4] Kubinová S, Syková E. Biomaterials combined with cell therapy for treatment of
10 spinal cord injury. *Regen Med* 2012;7:207–24.
- 11
- 12 [5] Straley KS, Foo CWP, Heilshorn SC. Biomaterial design strategies for the treatment of
13 spinal cord injuries. *J Neurotrauma* 2010;27:1–19.
- 14
- 15 [6] Wang M, Zhai P, Chen X, Schreyer DJ, Sun X, Cui F. Bioengineered scaffolds for
16 spinal cord repair. *Tissue Eng Part B* 2011;17:177–94.
- 17
- 18 [7] Talac R, Friedman JA, Moore MJ, Lu L, Jabbari E, Windebank AJ, et al. Animal
19 models of spinal cord injury for evaluation of tissue engineering treatment strategies.
20 *Biomaterials* 2004;25:1505–10.
- 21
- 22 [8] Chen BK, Knight AM, Madigan NN, Gross L, Dadsetan M, Nesbitt JJ, et al.
23 Comparison of polymer scaffolds in rat spinal cord: a step toward quantitative
24 assessment of combinatorial approaches to spinal cord repair. *Biomaterials*
25 2011;32:8077–86.
- 26
- 27 [9] Morrison B, Saatman KE, Meaney DF, McIntosh TK. In vitro central nervous system
28 models of mechanically induced trauma: a review. *J Neurotrauma* 1998;15:911–28.
- 29
- 30 [10] Krassioukov AV, Ackery A, Schwartz G, Adamchik Y, Liu Y, Fehlings MG. An in
31 vitro model of neurotrauma in organotypic spinal cord cultures from adult mice. *Brain*
32 *Res Protoc* 2002;10:60–8.
- 33
- 34 [11] Russell WMS, Burch RL. The principles of humane experimental technique. London:
35 Methuen & Co. Ltd; 1959.
- 36
- 37 [12] Daviaud N, Garbayo E, Schiller PC, Perez-Pinzon M, Montero-Menei CN.
38 Organotypic cultures as tools for optimizing central nervous system cell therapies. *Exp*
39 *Neurol* 2013;248:429-40.
- 40
- 41 [13] Spaethling JM, Geddes-Klein DM, Miller WJ, von Reyn CR, Singh P, Mesfin M, et al.
42 Linking impact to cellular and molecular sequelae of CNS injury: modeling in vivo
43 complexity with in vitro simplicity. *Prog Brain Res* 2007;161:27–39.
- 44
- 45 [14] Yiu G, He Z. Glial inhibition of CNS axon regeneration. *Nat Rev Neurosci*
46 2006;7:617–27.
- 47
- 48 [15] Neumann H, Kotter MR, Franklin RJM. Debris clearance by microglia: an essential
49 link between degeneration and regeneration. *Brain* 2009;132:288–95.
- 50
- 51
- 52
- 53
- 54
- 55
- 56
- 57
- 58
- 59
- 60
- 61
- 62
- 63
- 64
- 65

- 1
2
3
4
5
6
7
8
9
10
11
12
13
14
15
16
17
18
19
20
21
22
23
24
25
26
27
28
29
30
31
32
33
34
35
36
37
38
39
40
41
42
43
44
45
46
47
48
49
50
51
52
53
54
55
56
57
58
59
60
61
62
63
64
65
- [16] Loane DJ, Byrnes KR. Role of microglia in neurotrauma. *Neurotherapeutics* 2010;7:366–77.
 - [17] Zhou FQ, Snider WD. Intracellular control of developmental and regenerative axon growth. *Philos Trans R Soc Lond B Bio Sci* 2006;361:1575–92.
 - [18] Cho S, Wood A, Bowlby MR. Brain slices as models for neurodegenerative disease and screening platforms to identify novel therapeutics. *Curr Neuropharmacol* 2007;5:19–33.
 - [19] Ardelt AA, Flaris NA, Roth KA. Neurotrophin-4 selectively promotes survival of striatal neurons in organotypic slice culture. *Brain Res* 1994;647:340–4.
 - [20] Lohmann C, Ehrlich I, Friauf E. Axon regeneration in organotypic slice cultures from the mammalian auditory system is topographic and functional. *J Neurobiol* 1999;41:596–611.
 - [21] Lee, Y. B., Baratta, J., Yu, J., Lin, V. W., Robertson RT. aFGF Promotes Axonal Growth in Rat Spinal Cord Organotypic Slice Co-Cultures. *J Neurotrauma* 2002;19:357–67.
 - [22] Coltman BW, Earley EM, Shahar A, Dudek FE, Ide CF. Factors influencing mossy fiber collateral sprouting in organotypic slice cultures of neonatal mouse hippocampus. *J Comp Neurol* 1995;362:209–22.
 - [23] Jeong DK, Taghavi CE, Song KJ, Lee KB, Kang HW. Organotypic human spinal cord slice culture as an alternative to direct transplantation of human bone marrow precursor cells for treating spinal cord injury. *World Neurosurg* 2011;75:533–9.
 - [24] Kosuge Y, Sekikawa-Nishida K, Negi H, Ishige K, Ito Y. Characterization of chronic glutamate-mediated motor neuron toxicity in organotypic spinal cord culture prepared from ALS model mice. *Neurosci Lett* 2009;454:165–9.
 - [25] Duff K, Noble W, Gaynor K, Matsuoka Y. Organotypic Slice Cultures from Transgenic Mice as Disease Model Systems. *J Mol Neurosci* 2002;19:317–20.
 - [26] Dong HW, Buonomano DV. A technique for repeated recordings in cortical organotypic slices. *J Neurosci Methods* 2005;146:69–75.
 - [27] Marsh DR, Dekaban GA, Tan W, Strathdee CA, Weaver LC. Herpes simplex viral and amplicon vector-mediated gene transfer into glia and neurons in organotypic spinal cord and dorsal root ganglion cultures. *Mol Ther* 2000;1:464–78.
 - [28] Seidl AH, Rubel EW. A simple method for multi-day imaging of slice cultures. *Microsc Res Tech* 2010;73:37–44.
 - [29] Hailer NP, Vogt C, Korf HW, Dehghani F. Interleukin-1beta exacerbates and interleukin-1 receptor antagonist attenuates neuronal injury and microglial activation after excitotoxic damage in organotypic hippocampal slice cultures. *Eur J Neurosci* 2005;21:2347–60.

- 1
2
3
4
5
6
7
8
9
10
11
12
13
14
15
16
17
18
19
20
21
22
23
24
25
26
27
28
29
30
31
32
33
34
35
36
37
38
39
40
41
42
43
44
45
46
47
48
49
50
51
52
53
54
55
56
57
58
59
60
61
62
63
64
65
- [30] Cho JS, Park HW, Park SK, Roh S, Kang SK, Paik KS, et al. Transplantation of mesenchymal stem cells enhances axonal outgrowth and cell survival in an organotypic spinal cord slice culture. *Neurosci Lett* 2009;454:43–8.
 - [31] Bonnici B, Kapfhammer JP. Spontaneous regeneration of intrinsic spinal cord axons in a novel spinal cord slice culture model. *Eur J Neurosci* 2008;27:2483–92.
 - [32] Stoppini L, Buchs PA, Muller D. A simple method for organotypic cultures of nervous tissue. *J Neurosci Methods* 1991;37:173–82.
 - [33] Gähwiler BH, Capogna M, Debanne D, McKinney RA, Thompson SM. Organotypic slice cultures: a technique has come of age. *Trends Neurosci* 1997;20:471–7.
 - [34] Gähwiler BH. Organotypic monolayer cultures of nervous tissue. *J Neurosci Methods* 1981;4:329–42.
 - [35] Fawcett JW, Asher RA. The glial scar and central nervous system repair. *Brain Res Bull* 1999;49:377–91.
 - [36] Kadoya K, Tsukada S, Lu P, Coppola G, Geschwind D, Filbin MT, et al. Combined intrinsic and extrinsic neuronal mechanisms facilitate bridging axonal regeneration one year after spinal cord injury. *Neuron* 2009;64:165–72.
 - [37] Ruff CA, Wilcox JT, Fehlings MG. Cell-based transplantation strategies to promote plasticity following spinal cord injury. *Exp Neurol* 2012;235:78–90.
 - [38] Lu P, Yang H, Jones LL, Filbin MT, Tuszynski MH. Combinatorial therapy with neurotrophins and cAMP promotes axonal regeneration beyond sites of spinal cord injury. *J Neurosci* 2004;24:6402–9.
 - [39] Bradbury EJ, McMahon SB. Spinal cord repair strategies: why do they work? *Nat Rev Neurosci* 2006;7:644–53.
 - [40] Nomura H, Tator CH, Shoichet MS. Bioengineered strategies for spinal cord repair. *J Neurotrauma* 2006;23:496–507.
 - [41] Pêgo AP, Kubinova S, Cizkova D, Vanicky I, Mar FM, Sousa MM, et al. Regenerative medicine for the treatment of spinal cord injury: more than just promises? *J Cell Mol Med* 2012;16:2564–82.
 - [42] Boomkamp SD, Riehle MO, Wood J, Olson MF, Barnett SC. The development of a rat in vitro model of spinal cord injury demonstrating the additive effects of Rho and ROCK inhibitors on neurite outgrowth and myelination. *Glia* 2012;60:441–56.
 - [43] Kim HJ, Park JW, Byun JH, Vahidi B, Rhee SW, Jeon NL. Integrated microfluidics platforms for investigating injury and regeneration of CNS axons. *Ann Biomed Eng* 2012;40:1268–76.

- 1
2
3
4
5
6
7
8
9
10
11
12
13
14
15
16
17
18
19
20
21
22
23
24
25
26
27
28
29
30
31
32
33
34
35
36
37
38
39
40
41
42
43
44
45
46
47
48
49
50
51
52
53
54
55
56
57
58
59
60
61
62
63
64
65
- [44] Vahidi B, Park JW, Kim HJ, Jeon NL. Microfluidic-based strip assay for testing the effects of various surface-bound inhibitors in spinal cord injury. *J Neurosci Methods* 2008;170:188–96.
 - [45] Jin X, Ishii H, Bai Z, Itokazu T, Yamashita T. Temporal changes in cell marker expression and cellular infiltration in a controlled cortical impact model in adult male C57BL/6 mice. *PLoS One* 2012;7:e41892.
 - [46] Patist CM, Mulder MB, Gautier SE, Maquet V, Jérôme R, Oudega M. Freeze-dried poly(d,l-lactic acid) macroporous guidance scaffolds impregnated with brain-derived neurotrophic factor in the transected adult rat thoracic spinal cord. *Biomaterials* 2004;25:1569–82.
 - [47] Oudega M, Gautier SE, Chapon P, Fragoso M, Bates ML, Parel JM, et al. Axonal regeneration into Schwann cell grafts within resorbable poly(alpha-hydroxyacid) guidance channels in the adult rat spinal cord. *Biomaterials* 2001;22:1125–36.
 - [48] Maquet V, Martin D, Scholtes F, Franzen R, Schoenen J, Moonen G, et al. Poly(D,L-lactide) foams modified by poly(ethylene oxide)- block-poly(D,L-lactide) copolymers and a-FGF: in vitro and in vivo evaluation for spinal cord regeneration. *Biomaterials* 2001;22:1137–46.
 - [49] Hurtado A, Moon LDF, Maquet V, Blits B, Jérôme R, Oudega M. Poly (D,L-lactic acid) macroporous guidance scaffolds seeded with Schwann cells genetically modified to secrete a bi-functional neurotrophin implanted in the completely transected adult rat thoracic spinal cord. *Biomaterials* 2006;27:430–42.
 - [50] Hurtado A, Cregg JM, Wang HB, Wendell DF, Oudega M, Gilbert RJ, et al. Robust CNS regeneration after complete spinal cord transection using aligned poly-L-lactic acid microfibers. *Biomaterials* 2011;32:6068–79.
 - [51] Liesi P. Do neurons in the vertebrate CNS migrate on laminin? *EMBO J* 1985;4:1163–70.
 - [52] Menezes K, de Menezes JRL, Nascimento MA, Santos RDS, Coelho-Sampaio T. Polylaminin, a polymeric form of laminin, promotes regeneration after spinal cord injury. *FASEB J* 2010;24:4513–22.
 - [53] Tsai EC, Dalton PD, Shoichet MS, Tator CH. Matrix inclusion within synthetic hydrogel guidance channels improves specific supraspinal and local axonal regeneration after complete spinal cord transection. *Biomaterials* 2006;27:519–33.
 - [54] Cheng H, Huang YC, Chang PT, Huang YY. Laminin-incorporated nerve conduits made by plasma treatment for repairing spinal cord injury. *Biochem Biophys Res Commun* 2007;357:938–44.
 - [55] Wei YT, He Y, Xu CL, Wang Y, Liu BF, Wang XM, et al. Hyaluronic acid hydrogel modified with nogo-66 receptor antibody and poly-L-lysine to promote axon regrowth after spinal cord injury. *J Biomed Mater Res B Appl Biomater* 2010;95:110–7.

- 1
2
3
4
5
6
7
8
9
10
11
12
13
14
15
16
17
18
19
20
21
22
23
24
25
26
27
28
29
30
31
32
33
34
35
36
37
38
39
40
41
42
43
44
45
46
47
48
49
50
51
52
53
54
55
56
57
58
59
60
61
62
63
64
65
- [56] Rogers SL, Letourneau PC, Palm SL, McCarthy J, Furcht LT. Neurite extension by peripheral and central nervous system neurons in response to substratum-bound fibronectin and laminin. *Dev Biol* 1983;98:212–20.
 - [57] Gelain F, Panseri S, Antonini S, Cunha C, Donega M, Lowery J, et al. Transplantation of nanostructured composite scaffolds results in the regeneration of chronically injured spinal cords. *ACS Nano* 2011;5:227–36.
 - [58] Yang Y, Wimpenny I, Ahearne M. Portable nanofiber meshes dictate cell orientation throughout three-dimensional hydrogels. *Nanomedicine* 2011;7:131–6.
 - [59] Xie J, MacEwan MR, Schwartz AG, Xia Y. Electrospun nanofibers for neural tissue engineering. *Nanoscale* 2010;2:35–44.
 - [60] Wehrle R, Camand E, Chedotal A, Sotelo C, Dusart I. Expression of netrin-1, slit-1 and slit-3 but not of slit-2 after cerebellar and spinal cord lesions. *Eur J Neurosci* 2005;22:2134–44.
 - [61] Kitayama M, Ueno M, Itakura T, Yamashita T. Activated microglia inhibit axonal growth through RGMa. *PLoS One* 2011;6:e25234.

Figure 1. The production and lesioning of organotypic spinal cord slice cultures. (A) Schematic diagram depicting: (1) the slicing of murine spinal cords into 350 μm sections in the longitudinal sagittal plane and; (2) their transfer to culture inserts. (3) Following a defined culture period 'x', slices were lesioned with a double bladed scalpel by holding an elongated section (red arrow) of confetti (purple) together with the wall of the insert (grey) using forceps, thus keeping the slice stationary. (B) Photograph of the two scalpel blades, demonstrating equal blade spacing along the length of the blades. (C) Schematic diagram depicting: (1) electrospinning of aligned fluorescent poly-L,D-lactic acid nanofibers onto a parallel electrode collector; (2) the use of a densification tool (blue) to increase the line density of collected nanofibers; (3) attachment of portable acetate frames (black) containing spray adhesive to the aligned nanofibers on the densification tool (blue); (4) polymer coating of individual nanofiber frames in a specially designed chamber; (5) placement of aligned nanofiber frames over lesioned slices.

Figure 2. Characterization of spinal cord slices and induction of focal lesions. (A) Representative fluorescence micrograph of a live/dead-stained slice at 6 DIV, showing predominantly live cells in the main body of the slice with dead cells typically found at the slice edges (white arrowheads). (B) A slice stained with DAPI at 2 days post-lesioning, showing clear demarcation of lesion margins (white broken lines). (C) Bar chart of the distances between lesion margins, showing the reproducibility of the lesioning procedure across different experiments, each involving different slice preparations and freshly assembled lesioning tools ($n = 5$). (D) Representative live/dead stained fluorescence micrograph of a slice 5 days post-lesioning reveals some dead cells in lesion sites (white broken lines) with high viability in the main body of the slice.

Figure 3. Characterization of the cardinal features of SCI pathology in lesioned slices. (A) Representative fluorescence micrograph of a lesion margin 12 days post-lesioning shows intensely reactive astrocytes expressing an increase in GFAP (astrocyte marker; white arrowheads) expression and displaying hypertrophic morphologies (red arrowheads). The concomitant infiltration of rounded, lectin (microglial marker) expressing, activated microglia into the lesion site can be seen (white arrows). (B) Line graph of the optical density profiles for GFAP⁺ astrocytes in lesioned slices 7 days post-lesioning (mean profile in red; n = 6) showing a peak in expression at lesion margins. (C) Bar graph showing a significant difference between the average optical densities for GFAP⁺ slices between the first 100 μm from the lesion margins and two adjacent regions further into the slice body (**p < 0.01; n = 6). (D) Bar graph quantifying numbers of lectin⁺ microglia in lesion sites at 0, 5 and 10 days post-lesioning, demonstrating a peak in infiltration at 5 days (*p < 0.05, **p < 0.01; n = 3 per time point). (E) Representative fluorescence micrograph of extensive, random outgrowth of TUJ-1⁺ (pan-neuronal marker) nerve fibers in lesions in young slices (P0; lesioned after 1 DIV; stained 7 days later). (F) Representative fluorescence micrograph of relatively limited, random outgrowth of TUJ-1⁺ nerve fibers in older slices (P5; lesioned after 8 DIV; stained 7 days later).

Figure 4. Assessment of the cellular responses in lesions after placement of nanofibers over injured slices. (A) Photograph of aligned fluorescent nanofibers adhered to portable acetate frames. (B) Representative fluorescence micrograph of aligned nanofibers adhered to portable acetate frames. (C) Fluorescence micrograph showing placement of portable, aligned, uncoated nanofibers over a lesioned slice. (D) Live/dead staining of a lesioned slice 3 days after placement of aligned uncoated nanofibers, verifying safe nanofiber-placement procedures (white arrowheads mark cells likely to be in contact with nanofibers across the lesion). (E)

Representative fluorescence micrograph of GFAP⁺ scar-forming astrocytes shows no interaction with aligned uncoated nanofibers. (F) Representative fluorescence micrograph showing the attachment, outgrowth and alignment of scar-forming GFAP⁺ astrocytes on poly-D-lysine/laminin coated nanofibers across slice lesions. (G) Representative fluorescence micrograph showing attachment and alignment of lectin⁺ microglia to uncoated nanofibers.

Figure 5. The effect of nanofiber coating on the outgrowth and alignment of TUJ-1⁺ nerve fibers. (A) Representative fluorescence micrographs of the same field showing limited attachment and alignment of TUJ-1⁺ nerve fibers (left-hand panel) to uncoated aligned nanofibers (right-hand panel) in an ‘older’ lesion model displaying limited intrinsic regeneration (P5 slices; lesioning and nanofiber placement after 8 DIV; fixed 7 days later). (B) Representative fluorescence micrographs of the same field showing extensive outgrowth and alignment of TUJ-1⁺ nerve fibers (left-hand panel) on aligned coated nanofibers (right-hand panel) in the same lesion model as in (A). (C) Bar chart quantifying TUJ-1⁺ nerve fiber outgrowth density across lesions with un-coated and coated nanofiber (NF) treatment groups, compared to controls without nanofibers, in both ‘younger’ (P0 slices; lesioned after 1 DIV) and ‘older’ (P5 slices; lesioned after 8 DIV) slice models (**p < 0.01, ***p < 0.001). (D) Bar graph showing the distributions in scores of TUJ-1⁺ nerve fiber alignment for both un-coated and coated nanofiber treatment groups in both younger and older models. (E) Representative fluorescent micrograph of a likely TUJ-1⁺ interneuron at the lesion margins of control slices (P5) without nanofibers. (F) Fluorescence micrograph showing incidences of TUJ-1⁺ nerve fiber contact-guidance with aligned GFAP⁺ astrocytes (white arrowheads) in lesions with coated nanofibers.

Figure 6. Schematic diagram illustrating the potential screening utility of a ‘neural injury-nanomaterial’ interface paradigm.

Figure 1
[Click here to download high resolution image](#)

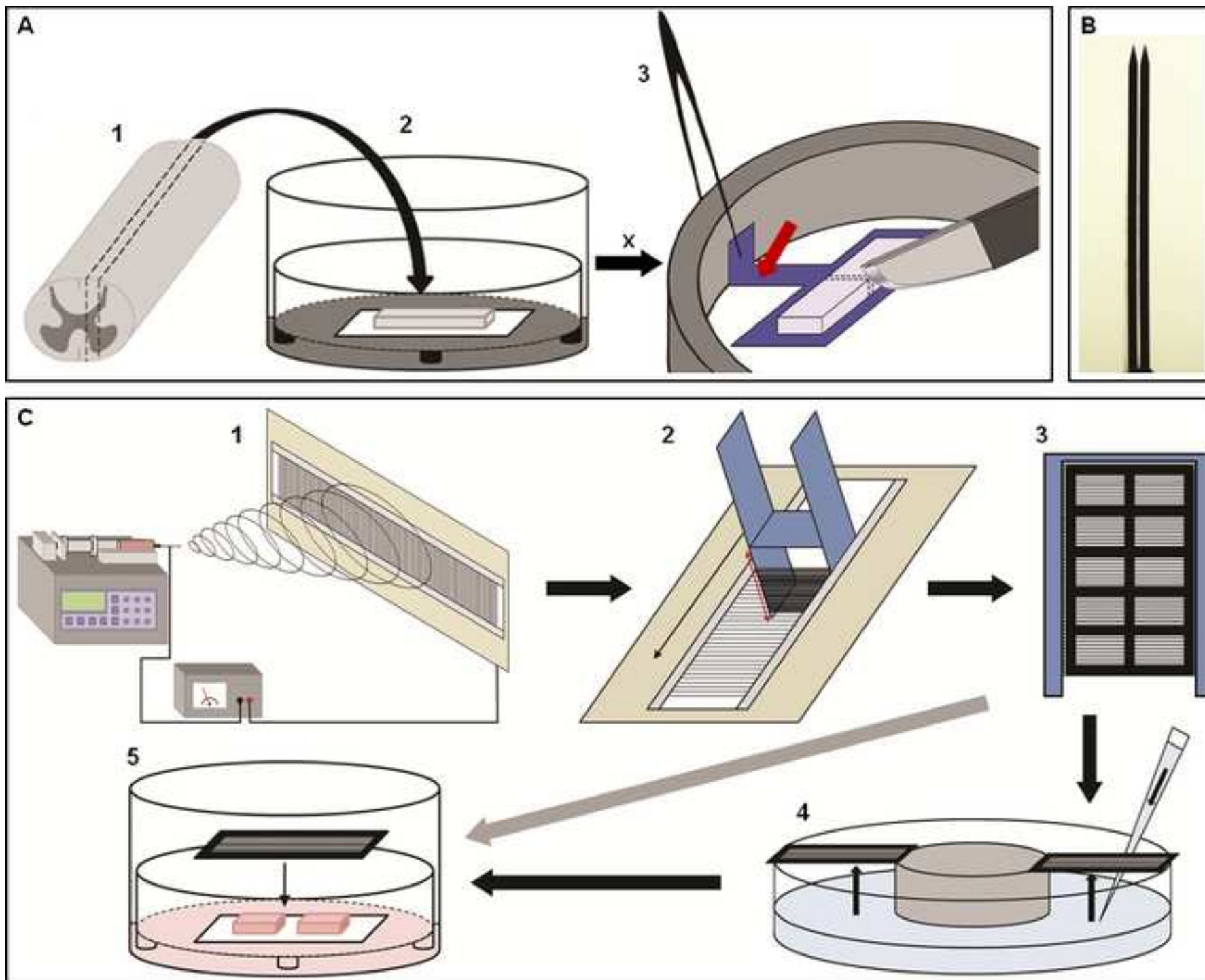


Figure 2
[Click here to download high resolution image](#)

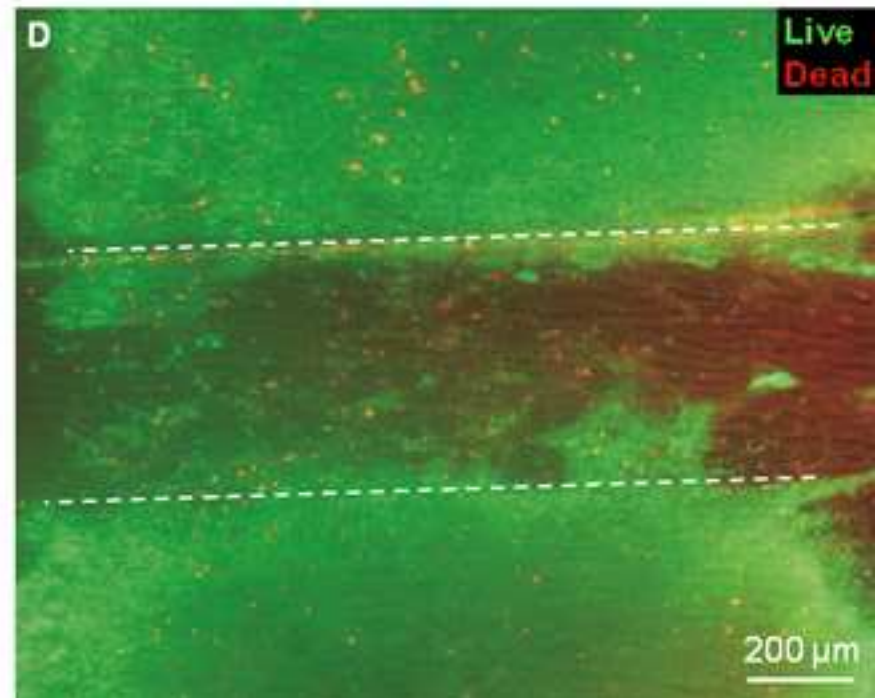
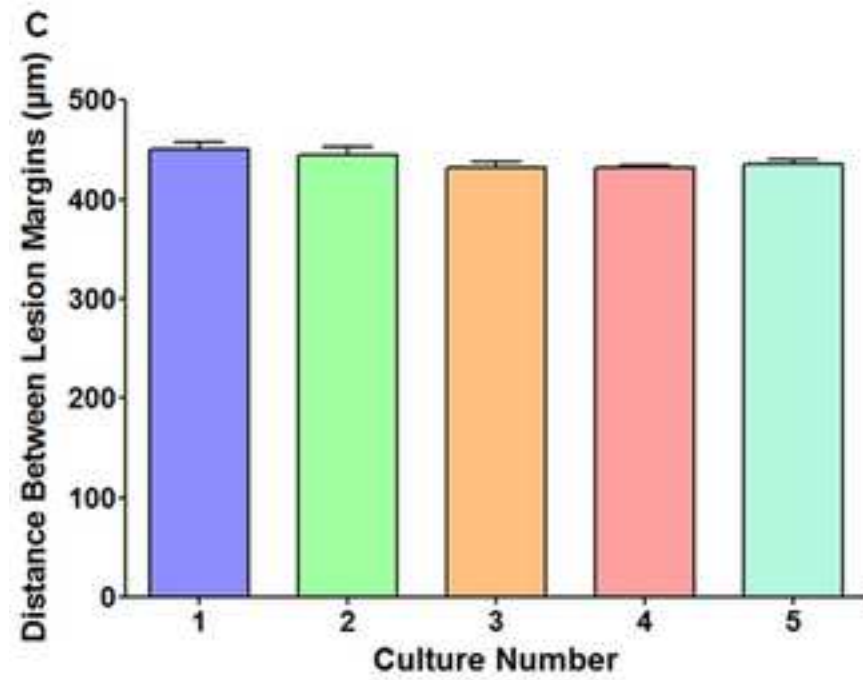
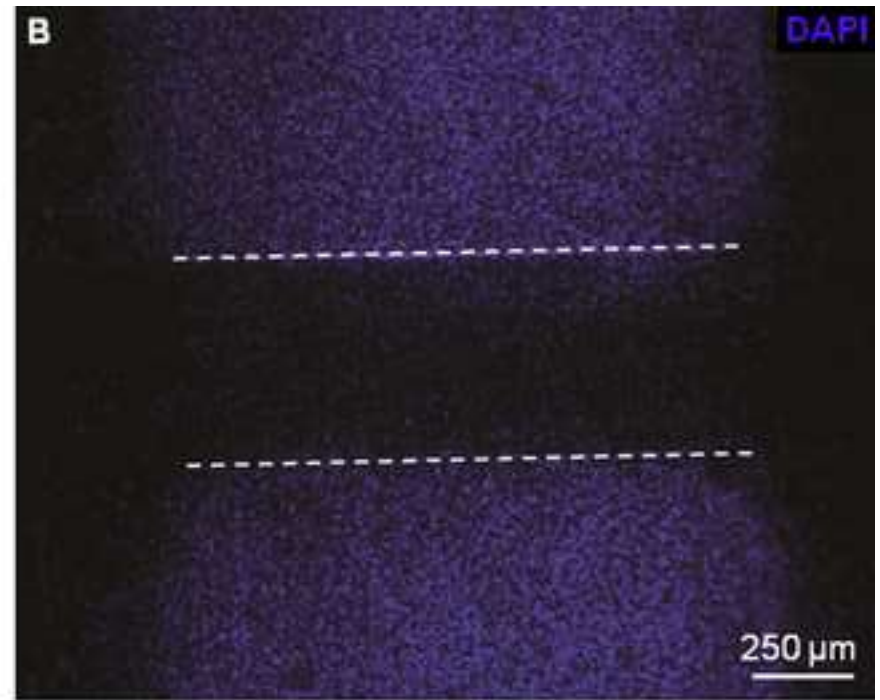
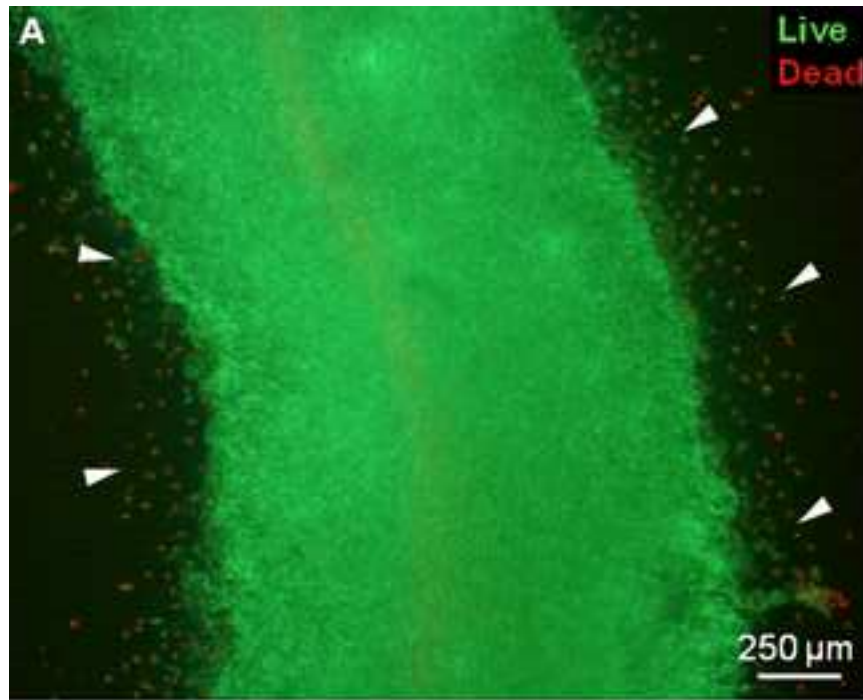


Figure 3
[Click here to download high resolution image](#)

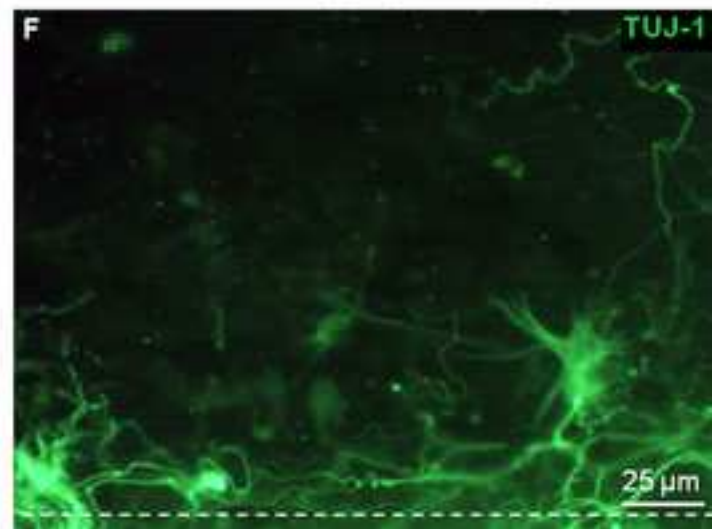
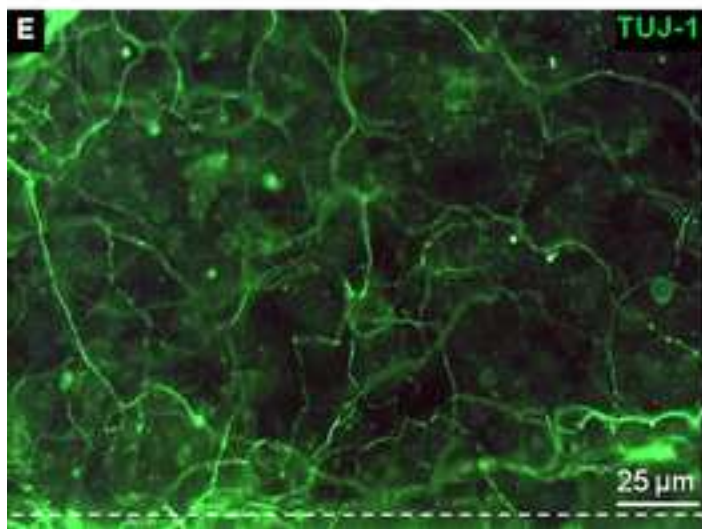
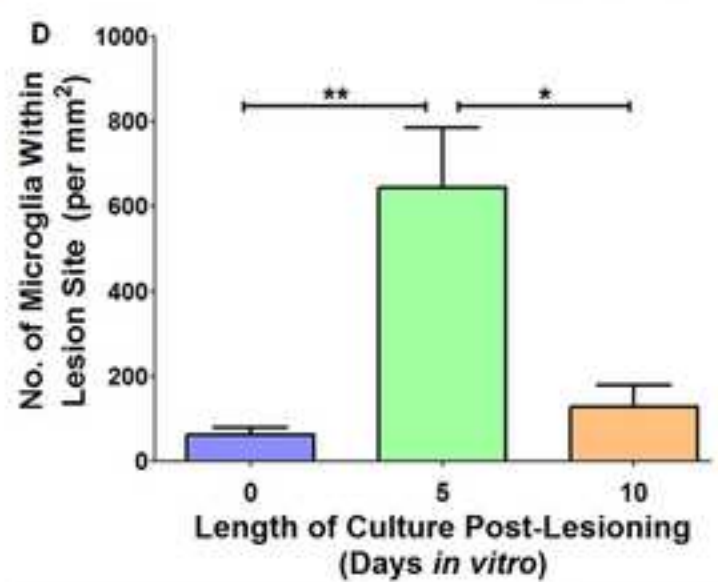
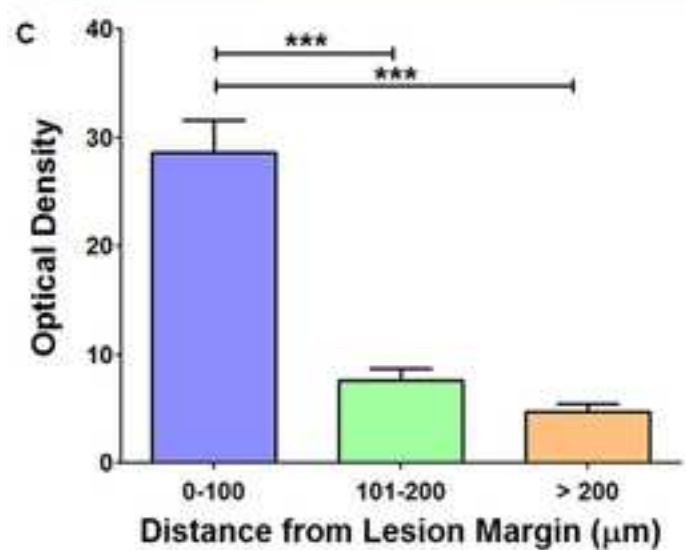
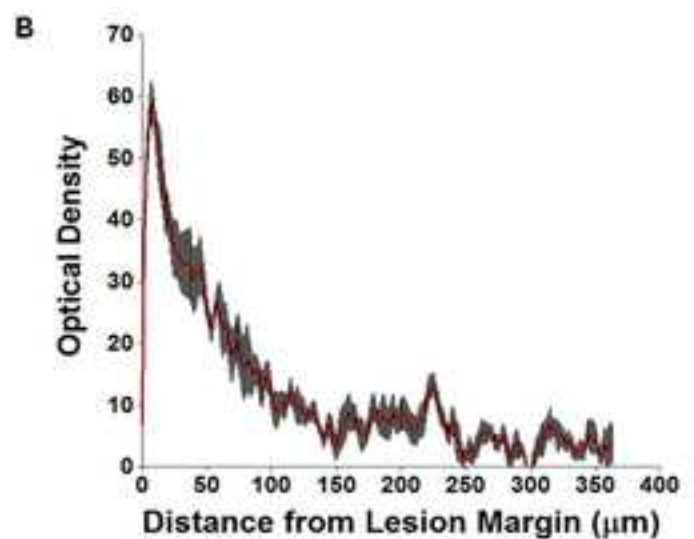
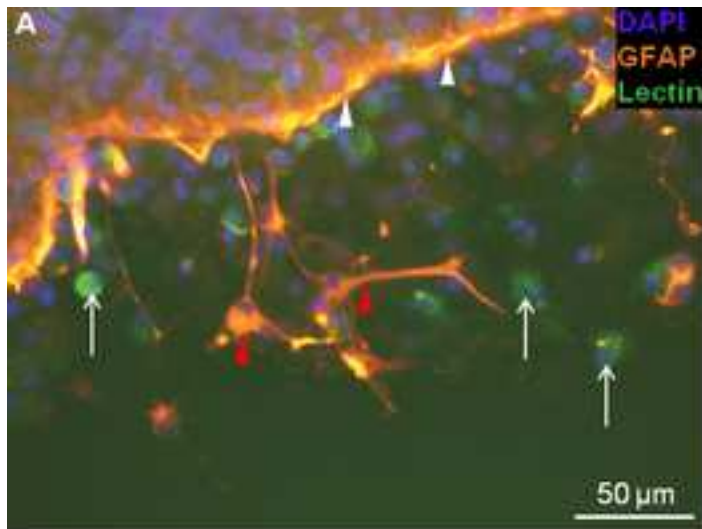


Figure 4
[Click here to download high resolution image](#)

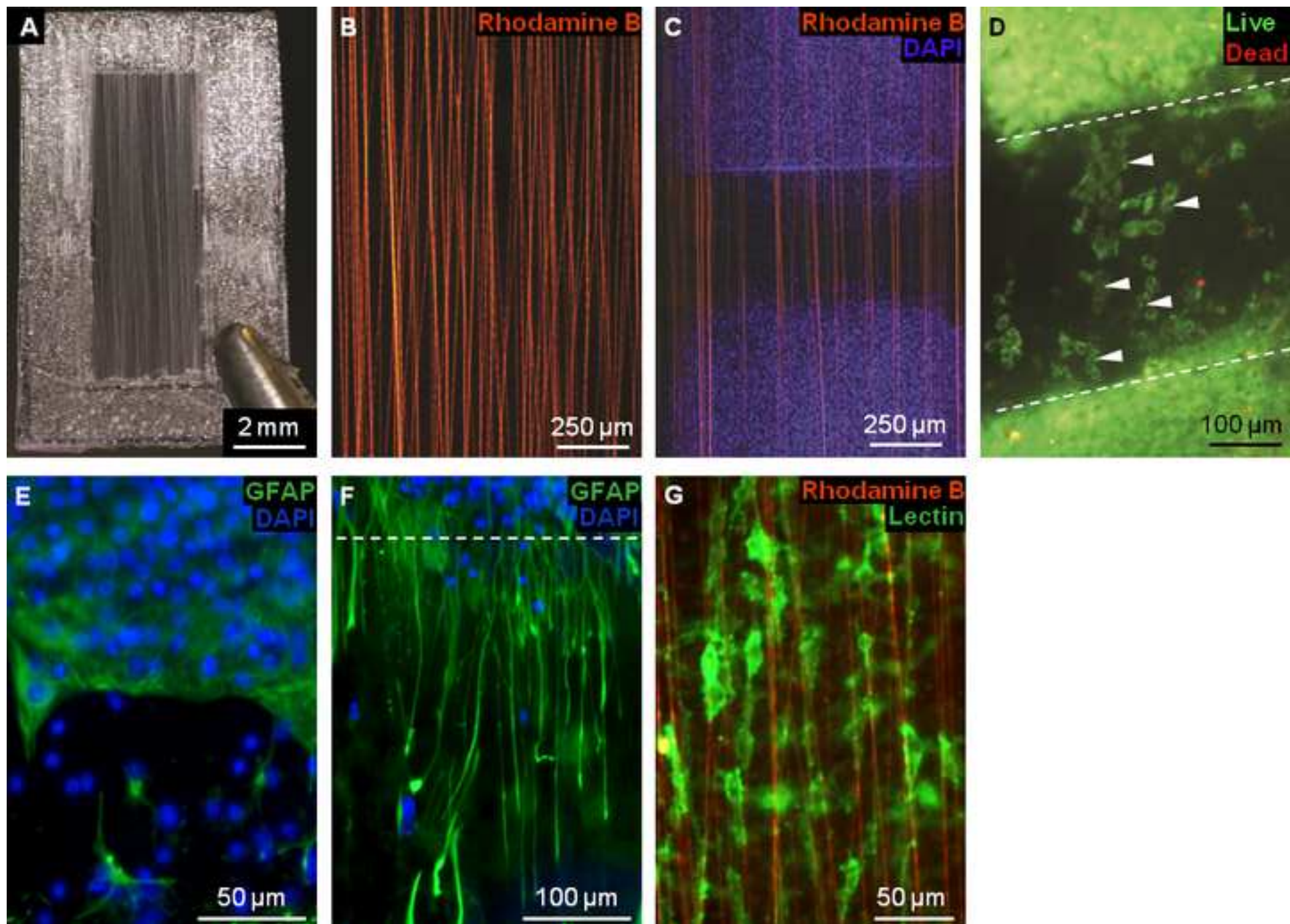


Figure 5
[Click here to download high resolution image](#)

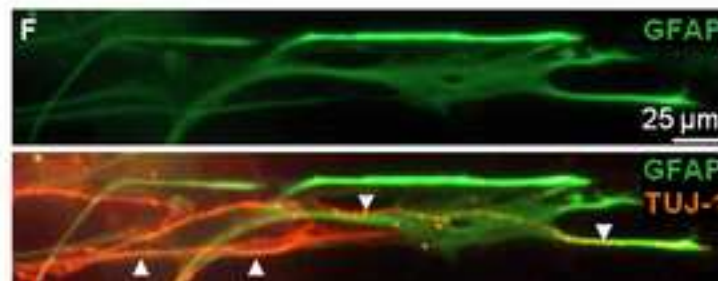
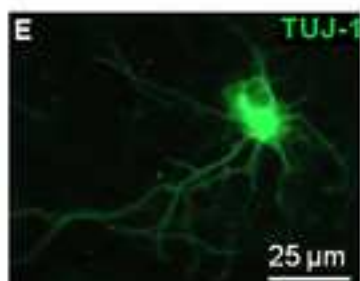
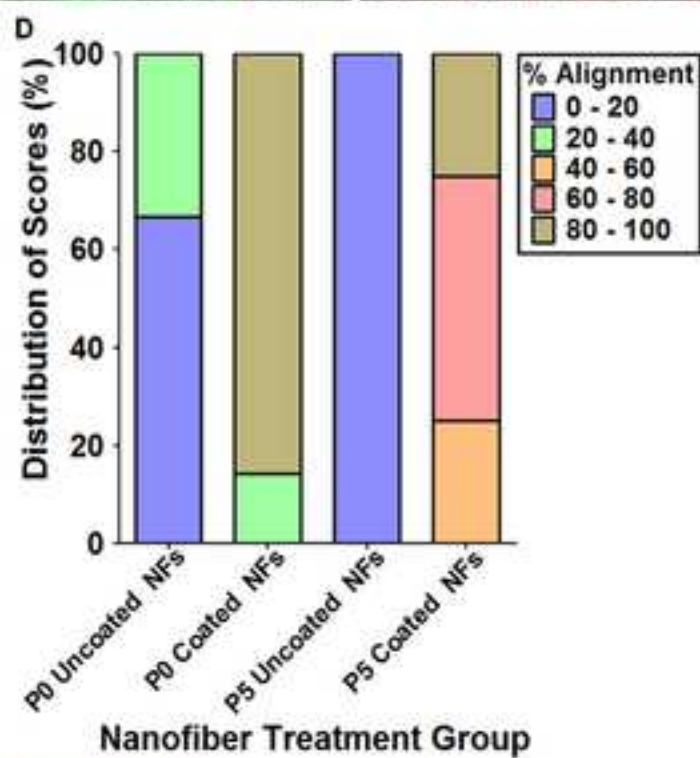
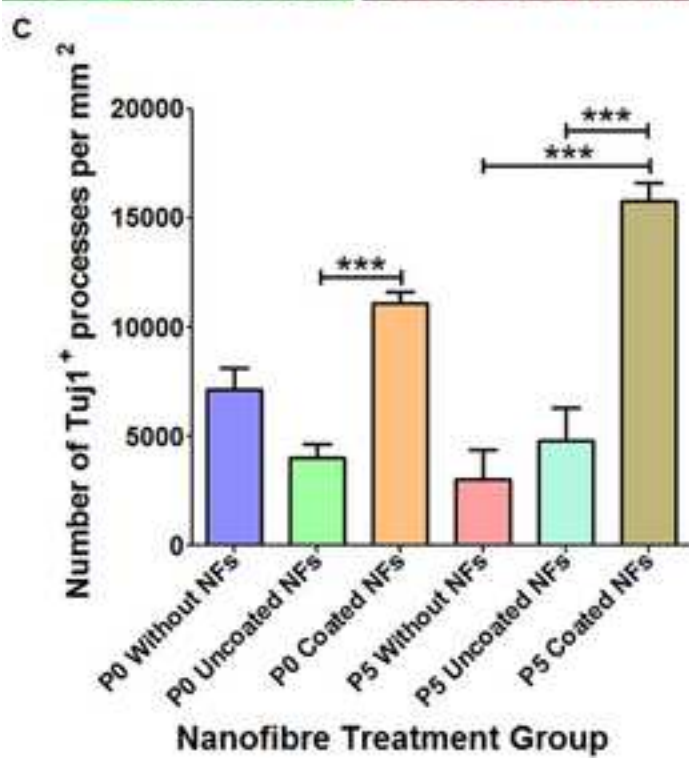
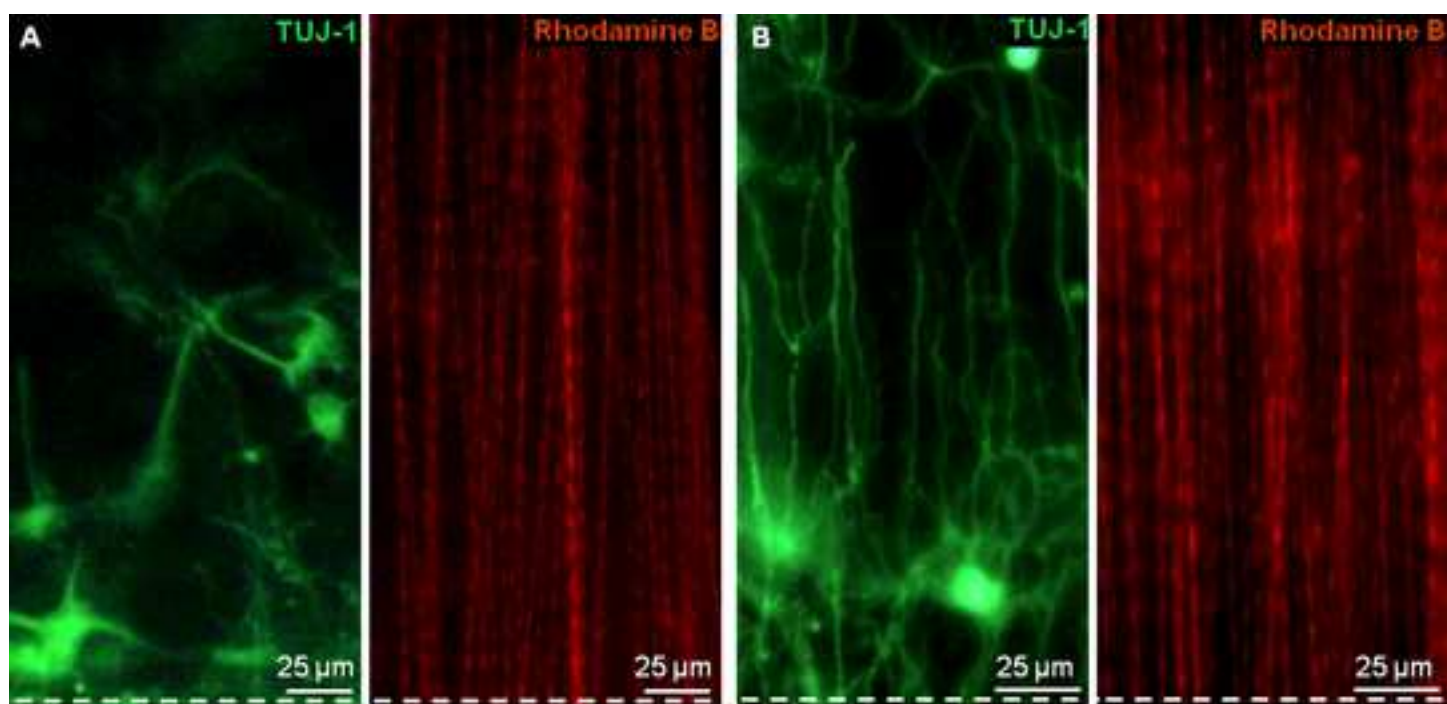
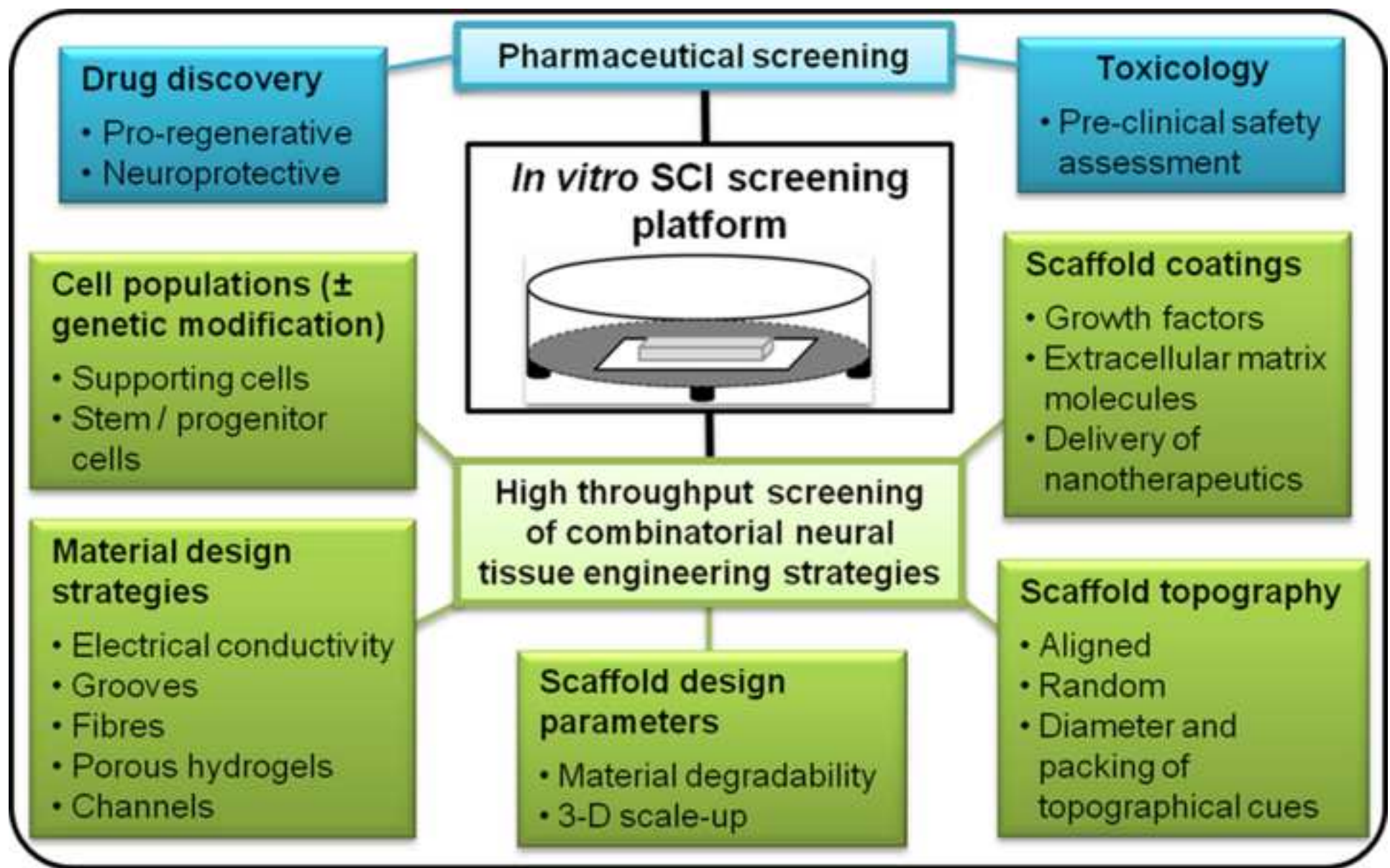


Figure 6
[Click here to download high resolution image](#)



Supplementary Files

[Click here to download Supplementary Files: Weightman et al. Supporting Info.docx](#)